Ceramics International 50 (2024) 52228–52239

Contents lists available at ScienceDirect

Ceramics International

journal homepage: www.elsevier.com/locate/ceramint

Investigation on melt growth (Mg, Co, Ni, Cu, Zn)O oxide ceramics prepared by laser directed energy deposition

Dongjiang Wu [a], Weijie Lv [a], Zheng Li [a], Xuexin Yu [a], Cong Zhou [b], Bi Zhang [b], Wei Wang [c], Huanyue Zhang [d], Guangyi Ma [a], Fangyong Niu [a,*]

[a] State Key Laboratory of High-performance Precision Manufacturing, Dalian University of Technology, Dalian, Liaoning, PR China
[b] Department of Mechanical and Energy Engineering, Southern University of Science and Technology, Shenzhen, Guangdong, PR China
[c] Department of Urology, Central Hospital of Dalian University of Technology, Dalian, Liaoning, PR China
[d] Instrumental Analysis Center, Dalian University of Technology, Dalian, Liaoning, PR China

ARTICLE INFO

Handling Editor: Dr P. Vincenzini

Keywords:
Additive manufacturing
Laser directed energy deposition
High entropy ceramic
Oxide ceramics

ABSTRACT

High-entropy oxides (HEOs) have attracted extensive research interest due to their unique structural features, customizable elemental compositions, and tunable functional properties. Nevertheless, the complexity, low efficiency, and high cost of the existing HEO synthesis methods place limitations on them. In this study, Laser directed energy deposition (LDED) was employed to synthesize (Mg, Co, Ni, Cu, Zn)O oxides. Additionally, the novelty of applying the LDED process to multicationic systems was emphasized. The comparison between specimens fabricated from mixed powder via LDED(MP) and those fabricated from pre-sintered powder via LDED (SP) encompasses macroscopic morphology, microstructure, and performance. The results showed that SP significantly enhanced the density from 86.44 % to 96.70 % compared to MP. The macro-segregation of Cu and Cu_2O in the phase composition was observed in MP and SP. High-temperature pre-sintering promoted the solid solution formation of Co and Ni during LDED, leading to more severe micro-segregation of Co and Ni. When employed as anodes in lithium-ion batteries, MP and SP have outstanding long-term cycle stability, according to electrochemical performance studies. At a current density of 100 mAg^{-1}, these specimens maintained a capacity retention rate of 100 % even after 200 cycles. The initial discharge capacities of MP and SP were respectively 477.73 mAh g^{-1} and 373.86 mAh g^{-1}. This study is expected to present a novel approach for the rapid synthesis of (Mg, Co, Ni, Cu, Zn)O oxide ceramics.

1. Introduction

High-entropy oxides (HEOs) are a unique class of inorganic non-metallic oxides composed of a solid solution of multiple elements, typically five or more, in equimolar or near-equimolar proportions. The lattice structure of HEOs represents a random mixture of these elements, distinct from the original lattice structures of the individual components. In 2015, Rost [1]was the first to successfully synthesize a single-phase $Mg_{0.2}Co_{0.2}Ni_{0.2}Zn_{0.2}Cu_{0.2}O$ high-entropy oxide by applying the design methodology of high-entropy alloys. This pioneering work introduced the concept and theoretical framework of 'high entropy' to oxide ceramics, laying the foundation for subsequent research on the synthesis, structural characteristics [2,3], and superior properties [4]of high-entropy oxides. HEOs have garnered significant attention for their exceptional electrochemical performance [5–10], particularly their impressive lithium-ion transport properties [11], with lithium-ion conductivity in Li-doped HEOs reaching approximately 10^{-3} S/cm. The micron-sized particles of HEO can exhibit long-term cycle stability and good rate performance as anodes for lithium-ion batteries [12]. The specific capacity of HEO nanoparticles can even be increased to more than 900 mAh g^{-1}, and the charge-discharge cycle can be more than 300 times. The future holds promise for the realization of solid-state batteries entirely based on HEOs.

The currently prevalent synthesis techniques for high-entropy oxides include solid phase sintering [1,5,13–15], spray pyrolysis [16], and co-precipitation [7,8,17]. High-entropy oxides prepared through solid-phase sintering exhibit excellent internal quality and performance characteristics. However, this fabrication method is complex and requires high sintering temperatures (over 1000 °C) and extended sintering times (exceeding 8 h). To enhance the material's quality and

* Corresponding author.
E-mail address: niufangyong@dlut.edu.cn (F. Niu).

https://doi.org/10.1016/j.ceramint.2024.10.029
Received 9 May 2024; Received in revised form 20 September 2024; Accepted 5 October 2024
Available online 5 October 2024

density, it is often necessary to apply high pressure or other auxiliary techniques. Alternatively, spray pyrolysis and co-precipitation methods are commonly employed for the preparation of high-entropy oxide powders. Among these, spray pyrolysis is particularly advantageous due to its high energy efficiency and ability to operate at lower temperatures. However, it requires stringent reaction conditions and temperatures, and the cost is high. Compared with the other two methods, the co-precipitation method has low experimental cost and simple equipment. It suffers from low deposition efficiency, and the precipitation and calcination conditions need to be strictly controlled. In summary, current methods for synthesizing high-entropy oxides typically involve complex processes, high costs, low production efficiencies, etc., and it is difficult to directly fabricate complex specimens.

Laser directed energy deposition (LDED) [18] is an additive manufacturing technique that employs a high-energy laser to completely melt high-melting-point materials for deposition and shaping. The technology melts material powders, enabling the in-situ deposition of melted materials to directly form three-dimensional structures. The 'near net forming' of complex specimens can be realized by LDED. It is distinguished by its straightforward process, high deposition efficiency, and short processing times, significantly enhancing fabrication efficiency [19]. LDED has not only been applied to high-entropy alloys such as AlCoCrFeNi [20–22] and CoCrFeMnNi [23–25] but has also been extended to the oxide ceramics. It has been applied to the fabrication of oxides such as Al_2O_3, Al_2O_3-YAG, and Al_2O_3-ZrO_2 [26–32]. The microhardness of melt-growth ceramics prepared using LDED can reach up to 2000 HV or more, and the flexural strength can reach up to 500 MPa. Part of the melt-growth ceramic properties comparable to those of ceramic materials prepared by traditional methods. The application of LDED in the field of high-entropy oxide ceramics holds significant importance. LDED is expected to introduce a novel alternative for the fabrication of high-entropy oxides.

In this work, (Mg, Co, Ni, Zn, Cu)O oxide ceramics were synthesized by LDED process using both mixed powder and pre-sintered powder. The microstructure, phase composition, and defects of specimens by LDED were analyzed. Electrochemical performance as anode for lithium-ion batteries was evaluated through cyclic voltammetry (CV) and charge-discharge curves. Additionally, the novelty of applying the LDED process to multicationic systems was emphasized. Our results demonstrate the feasibility of synthesizing these oxides using LDED, which is expected to advance the preparation of high-performance structural-functional high-entropy oxide ceramics through additive manufacturing.

2. Experimental process

2.1. Raw materials and treatment

2.1.1. Fabrication and characterization of mixed spherical powder

The raw materials of (Mg, Co, Ni, Zn, Cu)O prepared in this study are MgO (Aladdin, wt. % $\geq$ 99.9 %, particle size <1 μm), CoO (Aladdin, wt. % $\geq$ 99 %, particle size <1 μm), NiO (Aladdin, wt. % $\geq$ 99 %, particle size <1 μm), CuO (Aladdin, wt. % $\geq$ 99.5 %, particle size $\leq$50 nm), ZnO (Aladdin, wt. % $\geq$ 99.5 %, particle size 30 $\pm$ 10 nm). Five kinds of powders were mixed and granulated to meet the requirements of LDED powder shape and particle size.

The original powder was dried at 120 °C for 4 h before the fabrication of spherical powder to remove the moisture in the powder and prevent agglomeration or bonding. The process of fabricating spherical powder is as follows: The equimolar MgO, CoO, NiO, CuO, and ZnO powders were weighed and mixed on an electronic balance with an accuracy of 0.0001. A polyvinyl alcohol solution with a volume fraction of 5.12 % and a certain amount of anhydrous ethanol was added to the mixture. The mixture was milled in a planetary ball mill at a speed of 550 r/min for 5 h; so that all raw materials were fully mixed to obtain an oxide mixed slurry. Mixed spherical particles with particle size of 20 μm–70 μm were fabricated by centrifugal spray drying in Fig. 2(a). The inlet air temperature is 300 °C, the outlet air temperature is 120 °C, the frequency of the sprayer motor is 20–25 Hz, and the speed of the feed pump is 10–20 r/min. The mixed spherical particles were placed in a box-type sintering furnace and held at 500 °C for 30 min to remove the polyvinyl alcohol from the powder particles, resulting in pure mixed oxide spherical particles. The experimental process is illustrated in Fig. 1.

The morphology of the five kinds of original metal oxide powders is irregular, and the mixed spherical powders after granulation are spherical or ellipsoidal, as shown in Fig. 2. It shows that the equimolar mixed powder with good sphericity is obtained by centrifugal spray drying. The individual spherical powder particles consist of submicron and nanoparticle powders of the five aforementioned oxides. Due to the numerous gaps between the particles, the powder particles obtained through centrifugal spray drying are relatively loose. These gaps may lead to porosity during the LDED process, potentially increasing the occurrence of pore defects in the bulk specimens. The powder particles, ranging in size from 10 to 90 μm and shaped as spheres or ellipsoids, ensure good flowability, facilitating the smooth progress of LDED.

The SEM-EDS elemental surface distribution map of the equimolar mixed spherical powder is depicted in Fig. 3(a). The mapping shows that all spherical particles within the region contain the five metallic elements: Co, Cu, Ni, Zn, Mg, as well as the element O.The X-ray diffraction pattern of the spherical powder is shown in Fig. 3(b). It reveals the presence of the five metal oxides: CoO, MgO, ZnO, CuO, and NiO in the spherical powder, indicating that the centrifugal spray drying method can meet the requirements for a uniformly mixed composition of these five powders.

2.1.2. Fabrication and characterization of mixed pre-sintered powder

A portion of the mixed powder was sintered in a box-type furnace at 1000 °C for 10 h. Following the sintering process, the powder was rapidly removed from the furnace and subjected to air quenching. Due to the close contact between some powder particles during high-temperature sintering, sintering necks formed, resulting in slight agglomeration of the powder. To address this, the agglomerated powder was crushed. The morphology of the powder after pre-sintering and crushing is shown in Fig. 4. Even after being crushed into finer particles, the powder retained relatively good sphericity. Compared to the unsintered powder, the sintered powder became denser, with the submicron particles of the five oxides nearly indistinguishable. The five types of oxide powders have been bonded together after sintering. The particle size range of the powder is now 20–50 μm, and it retains good sphericity, meeting the requirements for LDED (see Fig. 5).

The SEM-EDS elemental surface distribution map of the sintered spherical powder is shown in Fig. 4. There is no significant difference in the types of elements between the pre-sintered powder and the unsintered powder, and no other elements are introduced during the sintering process. The atomic percentage of several atoms in the scanning area is shown in Table 1. The atomic percentage of O accounts for about 50 %, and the content of the other four metal atoms except Mg accounts for about 10 %, which is basically in line with the high entropy ceramic ratio. The density of MgO is relatively small, and a small amount of MgO may adhere to the inner wall of the container during ball milling and centrifugal spray drying, resulting in a small amount of defects.

2.2. Experimental equipment and process conditions

The laser directional energy deposition equipment mainly includes five parts: Nd: YAG laser (GSI Lumonics Company, UK), DPSF-2D two barrel powder feeder (Beijing Institute of Aeronautical Manufacturing Engineering, AVIC), CNC machine, industrial computers, and cooling water system.

In this experiment, constant process parameters were used: laser power 300 W, scanning speed 200 mm/min, interlayer lifting amount Δz

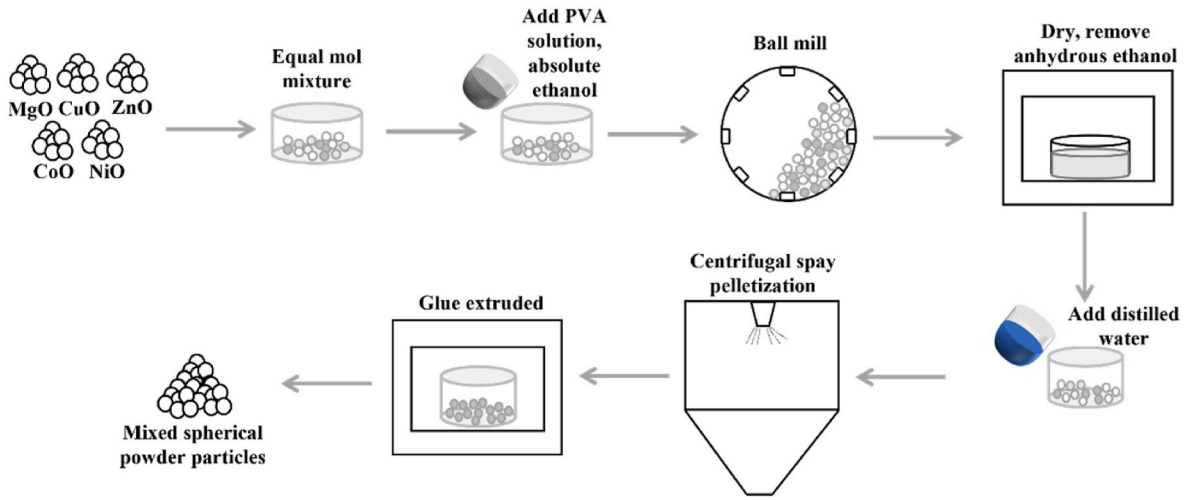

Fig. 1. Fabrication process of spherical powder.

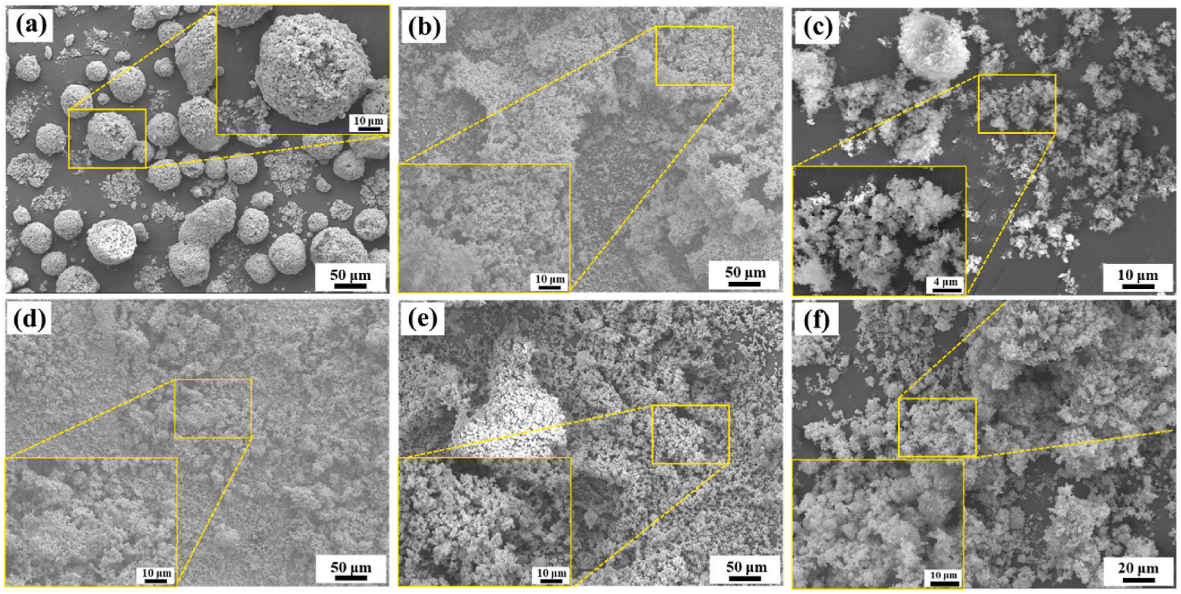

Fig. 2. The microstructure characteristics of mixed powder: (a) Spherical powder; (b) CoO; (c) MgO; (d) ZnO; (e) CuO; (f) NiO.

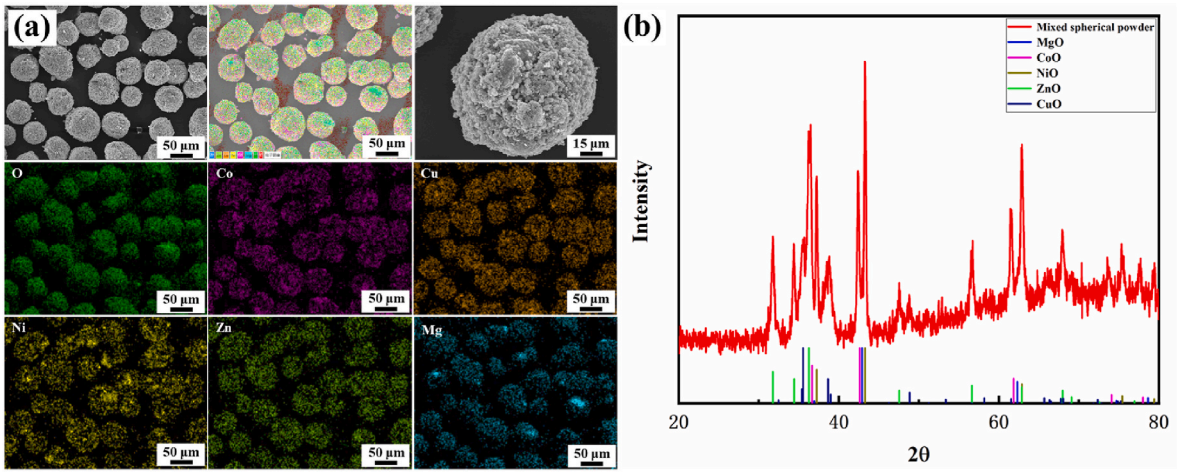

Fig. 3. Phase composition of mixed spherical powder: (a) Element distribution; (b) XRD patterns compared with CoO, MgO, ZnO, CuO, NiO five metal oxides.

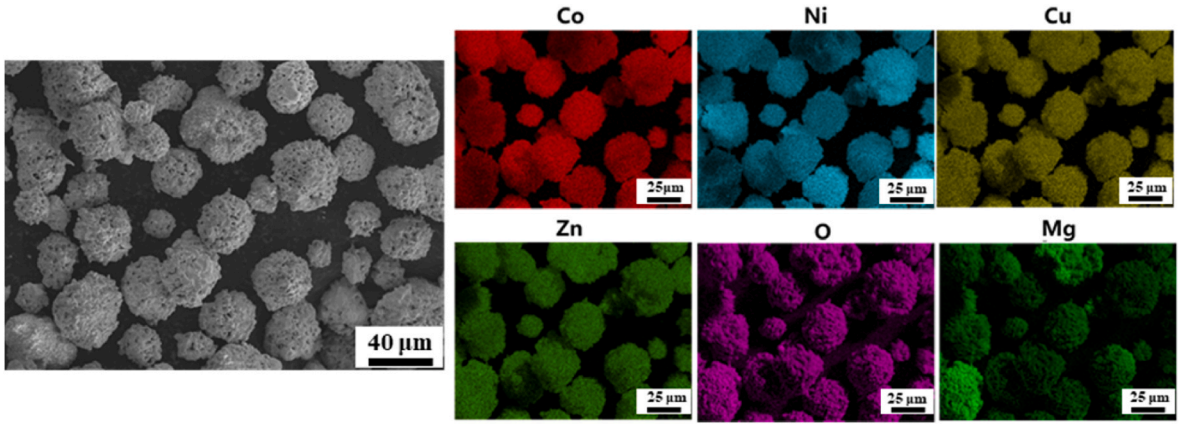

Fig. 4. Microstructure and element distribution of powder after pre-sintering and crushing.

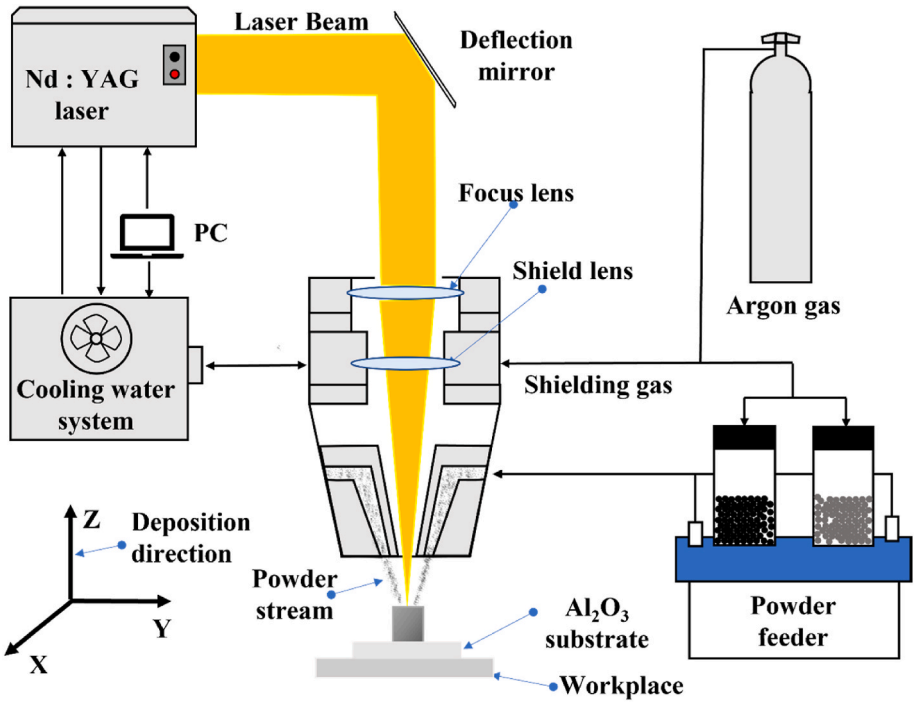

Fig. 5. Laser directed energy deposition system.

Table 1
Atomic percentage of powder after pre-sintering.

Element	O	Mg	Co	Ni	Cu	Zn
powder after pre-sintering	45.70 %	7.68 %	12.75 %	12.16 %	10.83 %	10.88 %
the nominal values	50 %	10 %	10 %	10 %	10 %	10 %

0.4 mm, and laser spot diameter 2 mm. The mixed spherical powder and the pre-sintered powder were deposited on the Al_2O_3 substrate by LDED to fabricate a cylindrical specimen with a diameter of 5 mm and a deposition height of 12 mm. High-purity argon gas (99.99 %) was used to deliver the uniformly mixed powder to the substrate. The laser beam, directed through deflecting mirrors and a focusing lens, reached the substrate. The coaxial powder was rapidly melted under the action of the Nd: YAG laser beam. For each deposition layer, the workbench dropped an interlayer lift Δz, and 30 layers were deposited to complete the fabricating of the cylindrical specimen. To ensure that the focus of the powder flow is located on the deposition surface during the fabricating process, the distance between the processing nozzle and the molten pool needs to be maintained at 9 mm.

2.3. Detection and analysis

Cylindrical specimens were cut from both the transverse and longitudinal sections. The surfaces for examination were prepared using standard metallographic techniques. Diamond sand discs (400#, 800#, 1500#, 2000#, 3000#) and 2.5 μm diamond abrasive paste were used to grind and polish the longitudinal and transverse sections of the specimens. The specimens and powders were analyzed for their physical phase composition by X-ray diffractometer (SHIMADZU, XRD-6000). The test conditions were incident beam Cu target Kα rays at a wavelength of 0.154178 nm, operating voltage and current of 40 kV and 30 mA, respectively, scanning speed of 4°/min, and scanning angle 2θ of 10°–80°. The microstructure and morphology of the powder were observed using an ultra-high resolution field emission scanning electron microscope (SEM, JEOL, JSM-7900F), and the elemental types and

contents of both the mixed and pre-sintered powders were analyzed using the EDS attached to the scanning electron microscope. The electron probe microanalyzer (EPMA, JEOL, JXA-8530F Plus) was utilized to analyze the elemental types and contents in specific areas of the specimens. Cross-sectional slices for TEM were prepared using a dual-beam focused ion beam workstation (FIB, Thermo Scientific, Helios G4 UX). These slices were further analyzed under a transmission electron microscope (TEM, JEM-2100F) at an acceleration voltage of 200 kV. High-resolution transmission electron microscopy (HRTEM) and selected area electron diffraction (SAED) were employed to characterize the different phases of the microstructure at the nanoscale. Temperature measurements were made using an infrared camera (FILR X6530sc) to measure the temperature of the LDED process. Porosity was quantified using Image Pro Plus software, which calculated the ratio of the pore area to the total cross-sectional area at the same deposition height across specimens, with an average taken from three specimens per group. Density was tested by Archimedes method, taking 9 specimens for 3 times and taking the average of 3 measurements. The theoretical density, $\rho_{theoretical}$, of the specimens was calculated based on the idealized uniform dispersion of metal elements in sublattice positions using formula (1) [33]:

$$\rho_{theoretical} = \frac{ZM}{N_A V} \tag{1}$$

Where Z is the number of molecules per unit cell, M is the molar mass of the material, N_A is Avogadro's constant, and V is the volume of the unit cell.

The volume-weighted average was calculated by using the regular mixing method through Eq. (2), and the coefficients of thermal expansion(CTE), $P_{composite}$, after equimolar mixing were calculated based on the CTE of the five materials, CoO, MgO, ZnO, CuO, and NiO [34].

$$P_{composite} = \sum (V_i \bullet P_i) \tag{2}$$

Where V_i is the volume fraction of the i-th component, and P_i is the CTE of the i-th component.

Cylindrical specimens prepared via LDED from both mixed and pre-sintered powders were ground into fine powder using a mortar and pestle. The battery performance of these powders as anode materials for lithium-ion batteries was evaluated using CR2032 button cells. The powder was mixed with conductive carbon black and polyvinylidene fluoride (PVDF) in a mass ratio of 8:1:1 and milled for 5 min. N-methylpyrrolidone (NMP) was then added to create a slurry, which was coated onto copper foil. The coated foil was dried on a heating table at 80 °C and subsequently placed in a vacuum oven at 100 °C for 8 h. The copper foil was cut into round pole pieces with a diameter of 12 mm. Celgard 2400 membrane was used as the separator, and the electrolyte consisted of LiPF6 solution. Electrochemical properties were tested by cyclic voltammetry (0.01–3 V, 0.1 mVs^{-1}) and charge/discharge cycling (0.01–3 V, 100 mAg^{-1}) on an electrochemical workstation (Neware CT-3008).

3. Results and discussion

3.1. Macro-morphology

The macro-morphology of cylindrical specimens formed by LDED from different powders is shown in Fig. 6. The color of the specimens is black, and the surfaces of each specimen formed from the various powders are rough, with unfused powder attached. To better combine the specimen with the substrate during the LDED, the first two layers were deposited at a slower scanning speed, resulting in a rough portion of about 1.5 mm at the lower end of the specimen. The diameter of the cylindrical specimen fabricated from mixed powder(MP) in Fig. 6(a) is 6.68 mm, which is slightly smaller than the diameter of the specimen fabricated from pre-sintered powder(SP) in Fig. 6(b), which is 7.72 mm.

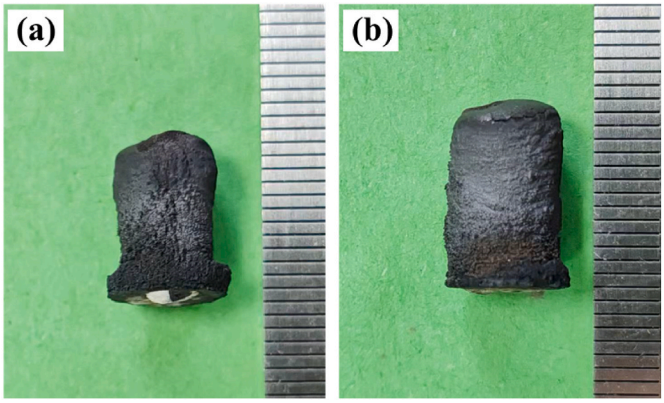

Fig. 6. Macro-morphology: (a) Mp; (b) SP.

The heights of the MP and SP are within the range of 13–14 mm because some residual powder from the powder delivery system enters the top of the melt pool after the laser ceases operation, resulting in the final specimen heights being greater than the preset height of 12 mm. After the laser stops, the top area undergoes rapid cooling from the high temperature area, and significant thermal stress appears at the top part, resulting in fine cracks at the top of the SP in Fig. 6 (b).

Table 2 shows the density of MP and SP. The density of SP is the highest, which can reach 96.70 ± 5.19 %, which is comparable to that of sintered specimens [33]; The minimum density of the MP is only 86.44 ± 5.35 %. To further determine the cause of the density gap, the pore defects of the cross-section of the specimen were counted. Pore defect is one of the main defects in the process of LDED forming ceramics, which has a great influence on the density of the specimen, and then affects the performance of the material. The cross-section porosity of the MP and SP was counted. As shown in Fig. 7 (a), there are many pores in the cross-section of the MP and most of them are distributed on the edge of the specimen. The porosity is 13.72 %, which is consistent with the measured density; Fig. 7 (b) shows the cross-section of the SP with a porosity of 4.7 %. The number of pores is much smaller than that of MP, but multiple cracks appear and are staggered. Fig. 7 (b) shows the cross-section of the SP, with a porosity of 4.7 %. The number of pores is much less than that of the sMP, but multiple cracks appear inside the specimen, which are staggered.

In the LDED deposition of cylindrical specimens, there are two main sources of pores: one is the gas inside the powder itself, spherical particles prepared by centrifugal spray granulation, the morphology is loose, and the gas inside the powder in the melt pool escapes into the melt pool. Two is the powder through the protective gas argon gas sent into the laser effect area to form a molten pool, in the molten pool under the action of the surface tension of the powder will carry part of the gas into the molten pool. Gas within the melt forms bubbles, which typically escape the melt pool through convection or buoyancy. However, during the rapid cooling process of the melt pool, these bubbles may become trapped, leading to the formation of pore defects. In the LDED process, the strong airflow from the protective gas during coaxial powder feeding exerts a downward force on the melt pool, inducing a clockwise circular motion that promotes convection. During this upward convection, bubbles are driven toward the edges of the melt pool. Consequently, larger and more numerous bubbles tend to accumulate at the specimen's edges before they can escape from the solid/liquid interface, resulting in

Table 2
Density of cylindrical specimens prepared by different powders.

	MP	SP
Volume density(g/cm^3)	5.3023 ± 0.2835	5.9333 ± 0.3082
Density	86.44 ± 5.35 %	96.70 ± 5.19 %

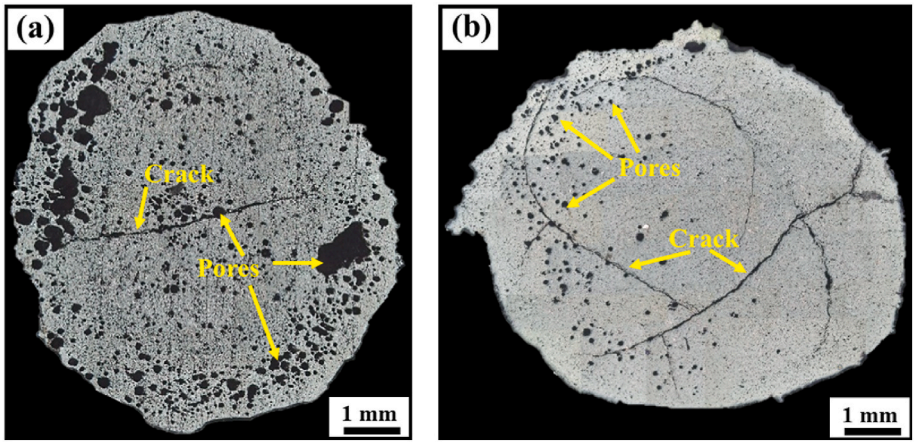

Fig. 7. Cross-sectional defects: (a) MP; (b) SP.

the formation of pores at the periphery.

The laser beam's high energy density, combined with the intrinsic brittleness of oxide ceramics due to their crystal structure and strong chemical bonds, makes the formation of crack defects likely during the LDED. The CTE of the material has a significant effect on the propagation of cracks. The CTE of the powder after pre-sintering is modified to $14.1 \times 10^{-6}\ K^{-1}$ [35]. Based on the CTEs of CoO, MgO, ZnO, CuO, and NiO [34], the calculated CTE of the mixed spherical powder using the rule of mixtures [36] is approximately $7.99 \times 10^{-6}\ K^{-1}$. Thus, the CTE of the pre-sintered powder is substantially higher than that of the mixed powder before modification. A high CTE indicates that the material will experience significant volume changes during heating or cooling processes. Such substantial thermal expansion and contraction can induce thermal stresses, which may result in cracking. During the LDED process, materials are subjected to multiple heating and cooling cycles, known as thermal cycling. For materials with a high CTE, these thermal cycles can cause severe thermal fatigue, further promoting crack propagation. Specimens fabricated from pre-sintered powder (SP) exhibit more cracks on their cross-sections compared to those fabricated from mixed powder using LDED.

3.2. Microstructure and phase composition

3.2.1. Microstructure

Fig. 8 shows the typical microstructures of MP and SP. As shown in Fig. 8(a) and (b), the microstructures of the transverse and longitudinal sections of MP exhibit irregularly shaped dark phases. These phases are continuously and uniformly distributed without any apparent pattern. The bright phases are evenly distributed within the dark phases, appearing as island-like or long strips. The shape of the bright phase depends to some extent on the shrinkage cavity formed by the solidification of the dark phase. As shown in Fig. 8(b), the bright hue is not a single phase, and one of the bright hues is completely embedded by the other. Fig. 8(c) and (d) display the microstructures of the transverse and longitudinal sections of SP. Different from MP, the dark phase has obvious micro-segregation, and the shape and distribution of the dark phase and the bright phase are almost the same.

Fig. 9 shows the results of map scanning element detection of MP and

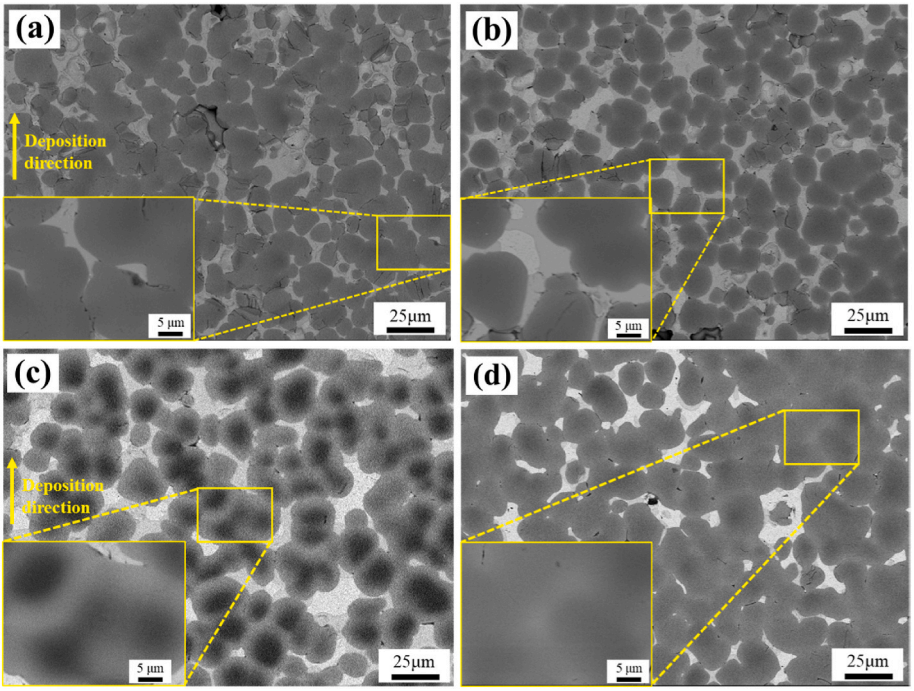

Fig. 8. Microstructure: (a) Longitudinal section of MP; (b) Cross-section of MP; (c) Longitudinal section of SP; (d) Cross-section of SP.

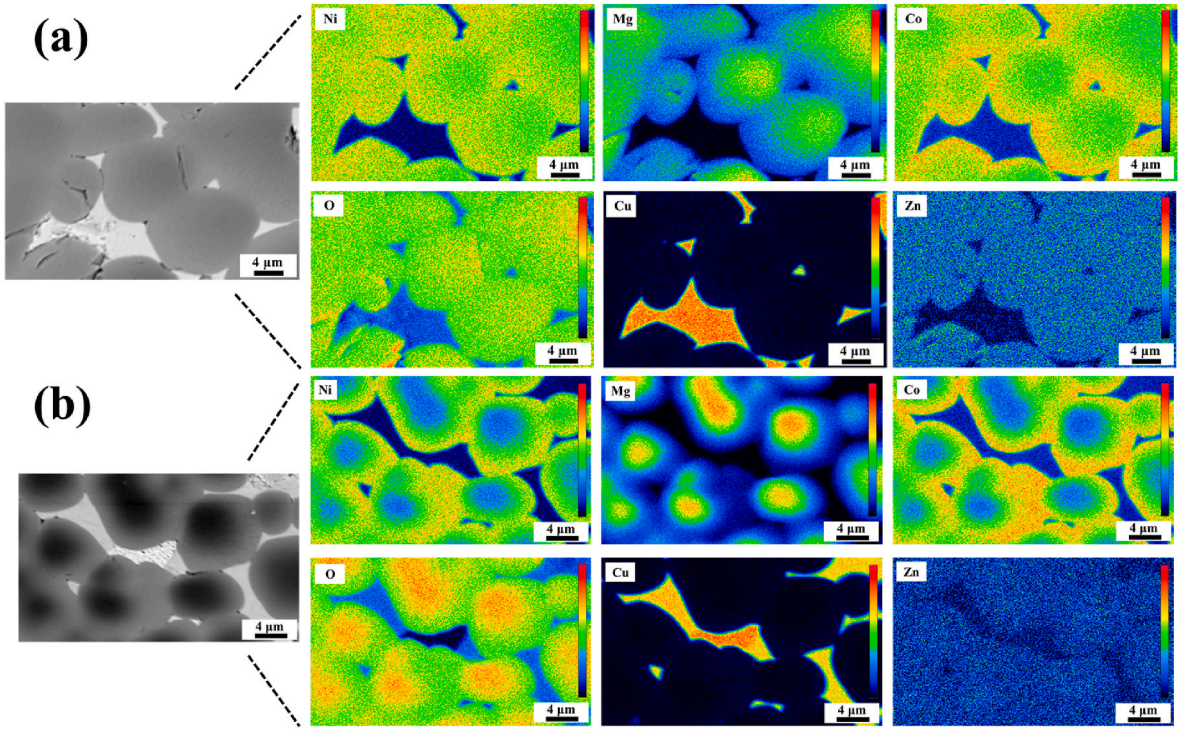

Fig. 9. EPMA map scanning: (a) MP; (b) SP.

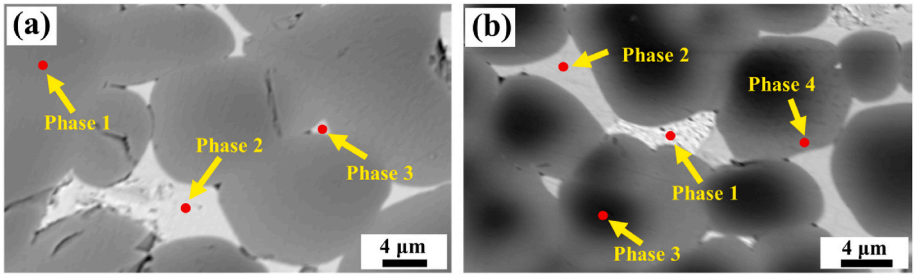

Fig. 10. EPMA spot scanning: (a) MP; (b) SP.

SP by EPMA. It can be seen from Fig. 9 that MP and SP are composed of six elements: Mg, Co, Ni, Cu, O, and a small amount of Zn. The bright phases are precipitated phase, both composed of Cu and O. However, the content of Cu and O varies between the two types of precipitated phase. In terms of macro-component segregation, there is no significant difference between MP and SP. The dark phase can be seen in the crystal group Co, and Ni gathered to the edge of the micro-segregation, the crystal group is mainly composed of Mg and O, but also contains a small amount of Co and Ni. The segregation of SP is more serious than that of MP (see Fig. 10).

3.2.2. *Macro-segregation*

Fig. 11 shows that the precipitated phases of MP and SP are composed of Cu and Cu_2O. During the melting and solidification process, CuO undergoes an in-situ reaction, being reduced to form Cu and Cu_2O. It can be mutually confirmed with the EPMA test results in Fig. 9, and two contrasts are shown in the precipitated phase. The brighter precipitated phase mainly contains Cu and almost no other elements; the darker precipitates mainly contain Cu and O. From the analysis of the atomic ratios of the elements given in Tables 3 and 4 combined with the results of the XRD patterns, it is concluded that the brighter precipitated phase corresponds to Cu and the darker precipitated phase is Cu_2O.

To more accurately determine the chemical composition and lattice

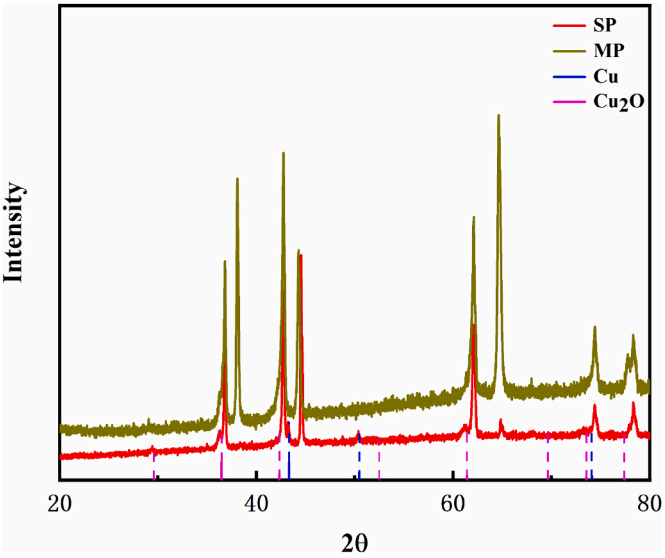

Fig. 11. X-ray diffraction patterns: (a) MP; (b) SP.

Table 3
Relative atomic percentage of each phase in MP.

	O	Cu	Zn	Mg	Co	Ni
Phase 1	38.42 %	1.09 %	2.22 %	10.78 %	23.90 %	23.58 %
Phase 2	1.49 %	91.48 %	0.23 %	0	4.59 %	2.21 %
Phase 3	21.77 %	70.50 %	0.71 %	0	4.46 %	2.56 %

Table 4
Relative atomic percentage of each phase in SP.

	O	Cu	Zn	Mg	Co	Ni
Phase 1	2.44 %	92.22 %	0.07 %	0.04 %	3.57 %	1.66 %
Phase 2	26.79 %	67.55 %	0.10 %	0	3.82 %	1.75 %
Phase 3	45.96 %	0.56 %	0.89 %	26.99 %	12.84 %	12.76 %
Phase 4	45.48 %	0.79 %	1.01 %	15.20 %	18.70 %	18.83 %

structure of the precipitated phase, TEM was used to analyze the atomic structure of MP and SP. The characteristic spacing of each crystalline surface obtained by combining selected area electron diffraction (SAED) and HRTEM image analysis is shown in Fig. 12. The cubic crystal system and its corresponding atomic layer spacing exhibited in Fig. 12(a) and (c), respectively, can correspond to the lattice parameters determined in the X-ray diffraction of Cu_2O. The face-centered cubic structure and the corresponding atomic layer spacing shown in Fig. 12 (b) and (d) are consistent with the lattice parameters determined by the X-ray diffraction pattern of the Cu. The diffraction images of MP and SP are different due to the different crystal belt axes selected during SAED.

The results of the infrared temperature measurement of LDED are shown in Fig. 13 (a). The maximum temperature of the molten pool is stable near 2100 °C. Due to the continuous heat input and the heat accumulation left after each layer of deposition, the temperature of the non-laser action zone can also reach more than 800 °C during LDED. In such a high temperature range, Cu^{2+} can be easily reduced to Cu^{+} [35] or Cu, and equation (3) and equation (4) reactions occur. The Gibbs free energy ΔG that may react in the forming temperature range is calculated to determine the tendency of the reaction. When ΔG < 0, the reaction proceeds spontaneously at this temperature and pressure, and the smaller ΔG indicates that the reaction tends to proceed spontaneously under this condition. As shown in Fig. 13(b), the reduction reaction from Cu^{2+} to Cu^{+} (Equation (3)) has the smallest ΔG, indicating a strong tendency for this reaction to occur in the initial stages. However, the reduction of Cu^{2+} to Cu (Equation (4)) also shows a negative ΔG, indicating that a minor amount of Cu^{2+} is involved in this reaction as well. Since every chemical reaction has an equilibrium constant, as the reaction progresses and the concentration of Cu^{+} increases, the tendency for this reaction to occur decreases. As the concentration of the products becomes higher, the reaction's driving force diminishes, leading to an increased tendency for the reduction of Cu^{2+} to elemental Cu, and more elemental Cu precipitates out of the molten pool. In thermodynamic calculations, the ΔG for the reaction converting Cu^{+} to Cu is greater than 0, indicating that this reaction is non-spontaneous at the given temperature. Therefore, it is unlikely to occur naturally, effectively ruling out the possibility of Cu^{+} being reduced to elemental Cu during the process. According to the results of EPMA, the content of Zn is significantly lower than the other four metallic elements. Under conditions of limited oxygen and high temperatures (above 1975 °C), ZnO first melts and then decomposes into metallic Zn and O_2. It is important to note that at these elevated temperatures, the metallic zinc produced by this decomposition rapidly evaporates due to zinc's high vapor pressure. This evaporation leads to the loss of zinc from the molten pool, as described by the reaction in Equation (5). The thermodynamic calculations shown in Fig. 13(b) further support this assertion. At a temperature of 2000 °C, the ΔG (change in Gibbs free energy) for the reaction is less than 0, indicating that the reaction, including the evaporation of Zn, can occur spontaneously.

$$4CuO = 2Cu_2O + O_2(g) \quad (3)$$

$$2CuO = 2Cu + O_2(g) \quad (4)$$

$$2ZnO = 2Zn(g) + O_2(g) \quad (5)$$

The schematic in Fig. 14 illustrates the process of macroscopic compositional segregation occurring during LDED. In the process of

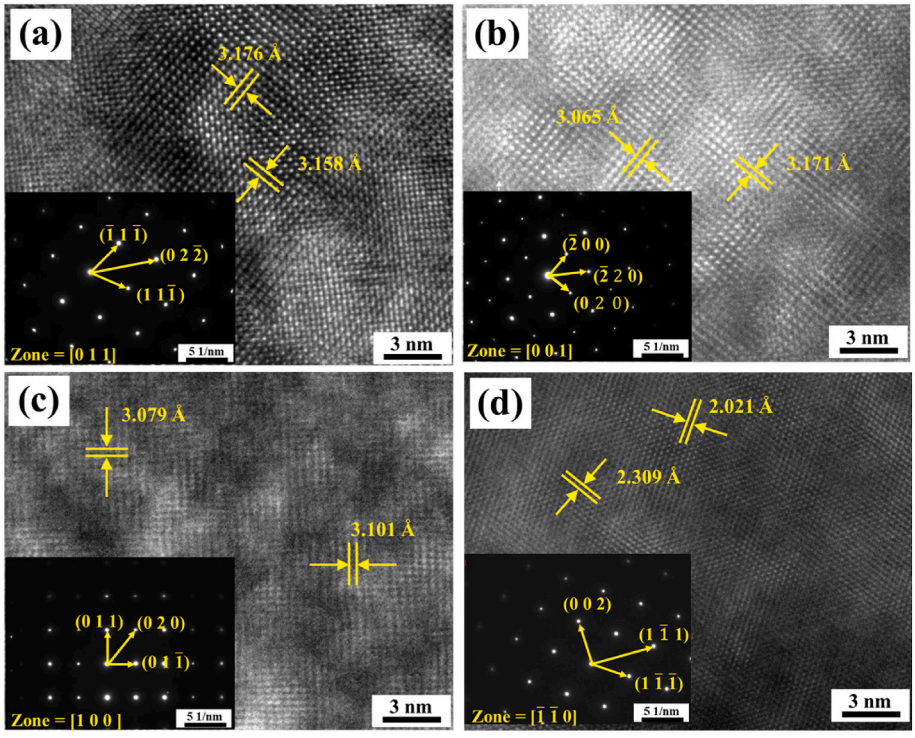

Fig. 12. HRTEM and SAED images of the precipitated phase: (a) MP; (b) SP.

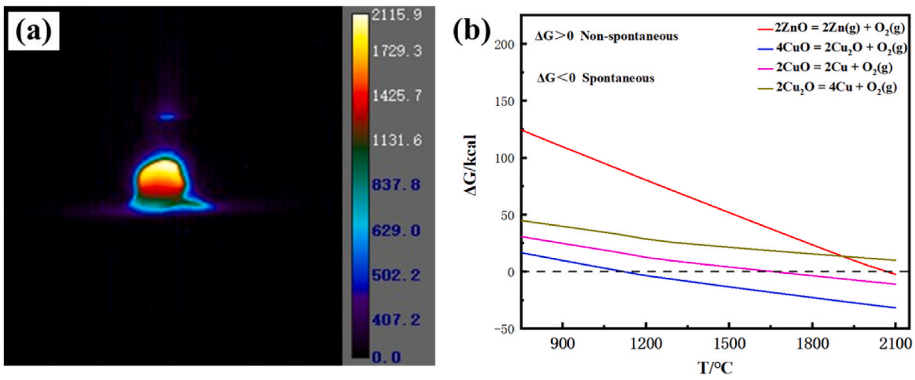

Fig. 13. Chemical reaction calculation of LDED forming process: (a) Infrared temperature measurement; (b) Thermodynamic calculation of chemical reaction.

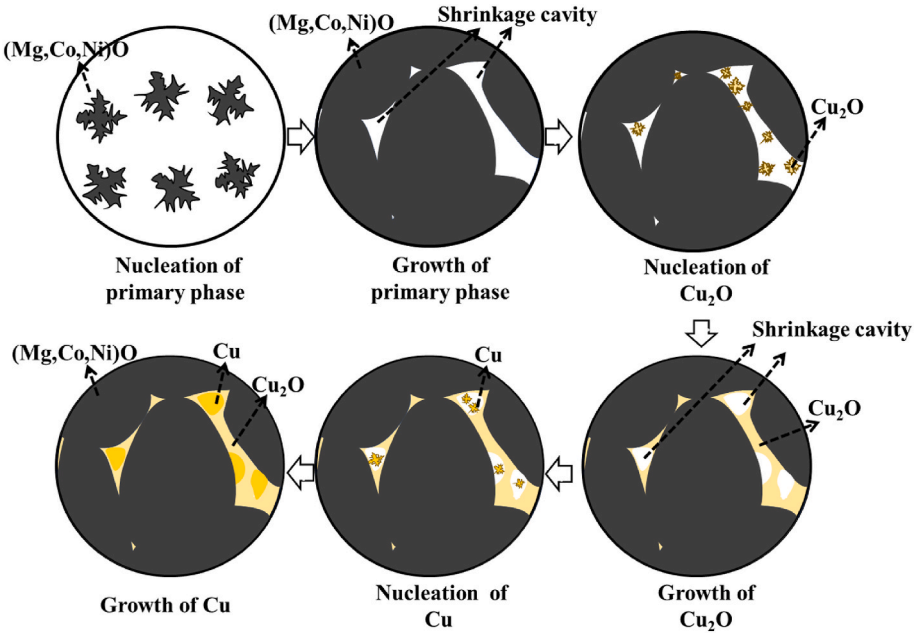

Fig. 14. Macro-segregation diagram of LDED.

LDED, materials within the laser-affected zone exist in a molten state within the melt pool. Driven by the temperature gradient of the surface tension within the melt pool, Marangoni convection occurs. It enhances the flow of the molten liquid inside the melt pool, facilitating the mixing and contact of different elements, which promotes chemical reactions. These reactions lead to the formation of Cu_2O, Cu, and Zn vapor. At the peak temperature within the melt pool, Zn vaporizes and escapes from the melt pool. During the solidification process, (Mg, Co, Ni)O has a higher melting entropy and tends to nucleate and grow first as the primary phase. Given that the melting point of Cu_2O (1235 °C) is higher than that of Cu (1085 °C), when the degree of undercooling is sufficient for the solidification of Cu_2O, it can nucleate heterogeneously on the already solidified (Mg, Co, Ni)O phases. This results in the nucleation and growth of Cu_2O along the surfaces of the (Mg, Co, Ni)O phases, effectively filling in the shrinkage cavity that formed during the solidification of primary phases. As cooling continues, Cu, having the lowest melting entropy among these materials, nucleates and grows last, ultimately precipitating out of the molten state.

3.2.3. *Micro-segregation*

According to the EPMA results shown in Fig. 9, significant micro-segregation is evident in the dark phases of MP and SP. There is a notable enrichment of Co and Ni at the boundaries of the dark phase crystallites. This micro-segregation is more pronounced in SP. As shown in Fig. 15, the atomic structure of phases 3 and 4 with micro-segregation was analyzed. Based on the Selected Area Electron Diffraction (SAED) patterns, it can be concluded that both phases 3 and 4 have the same crystal structure, which is face-centered cubic (FCC). There are slight differences in the distribution of elements within these phases. This confirms that phases 3 and 4 are the same phase, but segregation occurred during the solidification process. Apart from the precipitation of Cu and Cu_2O, no other new phases formed or precipitated.

According to Hume-Rothery rules [37], when two elements have similar atomic radii (with a difference of less than 15 %), the atoms of one element can more easily substitute the atoms of another without causing significant lattice distortion, thereby facilitating the formation of solid solutions. Co and Ni have very similar atomic radii, approximately 125 p.m. and 124 p.m., and both belong to the transition metals category. Due to their both typically exhibit a coordination number of 6 in octahedral complexes, they demonstrate excellent mutual solubility when forming solid solutions [38]. The atomic radius of Mg is approximately 160 p.m., which is significantly larger than those of Co and Ni. Due to this considerable difference in atomic size, magnesium has a lower tendency to form solid solutions with Co and Ni. This substantiate supports the findings from Table 4, where the Co to Ni content is nearly 1:1, indicating good intermiscibility. In regions with a higher

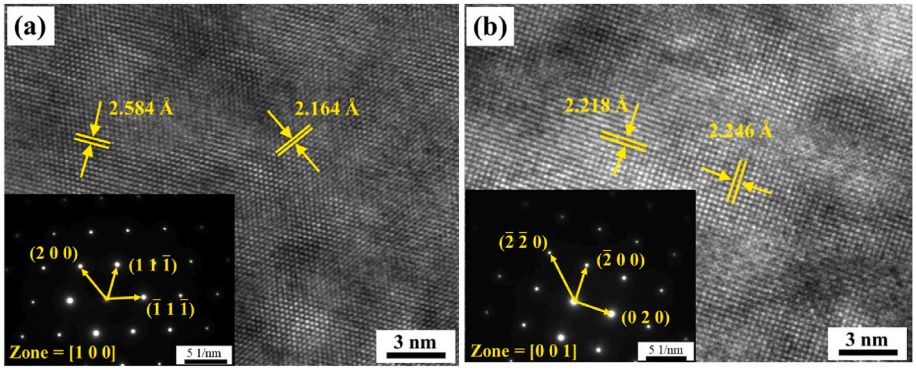

Fig. 15. HRTEM and SAED images of dark phase in SP: (a) Phase 3; (b) Phase 4.

concentration of Mg, the solubility of Co and Ni is reduced. The rapid cooling rates of LDED prevent Co and Ni from dissolving quickly during the cooling process. This leads to the enrichment of Co and Ni at the edges of the Mg-rich areas.

The increase in the CTE from 7.99×10^{-6} K^{-1} for the mixed powder to 14.1×10^{-6} K^{-1} for the pre-sintered powder reflects a significant modification in the material properties due to the pre-sintering process. This higher CTE means that the material undergoes greater expansion and contraction with temperature changes, which can generate larger thermal stresses during LDED. These increased thermal stresses exacerbate the thermal gradients within the melt pool. As a result, there are more pronounced temperature differences within the molten pool. According to the Boussinesq approximation, an increase in the CTE leads to greater density variations within the fluid, such as the molten pool in LDED, as shown in equation (6). These variations enhance thermal convection currents within the melt pool, promoting more thorough mixing and homogenization of the material. The larger CTE not only intensifies the thermal convection but also facilitates a more complete solid solution of Co and Ni during the rapid solidification process in SP. This results in more pronounced segregation of Co and Ni within the microstructure compared to MP.

$$\rho = \rho_0[1 - \alpha \bullet \Delta T] \tag{6}$$

Where ρ_0 is reference density, α is the CTE, and ΔT is the temperature gradient.

3.3. Comparison of electrochemical performance

Fig. 16(a) and (b) display the cyclic voltammograms of MP and SP within a voltage range of 0.01–3 V at a scan rate of 0.1 mV/s. In the initial cycle, the reduction curve in Fig. 16(a) shows three reduction peaks. The first peak, which does not reappear in subsequent cycles, occurs around 0 V, indicating a gradual increase in current due to electrolyte decomposition and the formation of the Solid Electrolyte Interface (SEI) layer on the electrode surface. As the SEI layer matures and thickens, the current subsequently decreases. These two irreversible reduction peaks contribute to the significant irreversible capacity loss observed in the charge-discharge cycles shown in Fig. 16(c). In the second and third cycles, the overlapping reduction and oxidation peaks suggest the recyclability of MP in the intercalation and deintercalation of Li^+. However, the peak current values increase with the number of

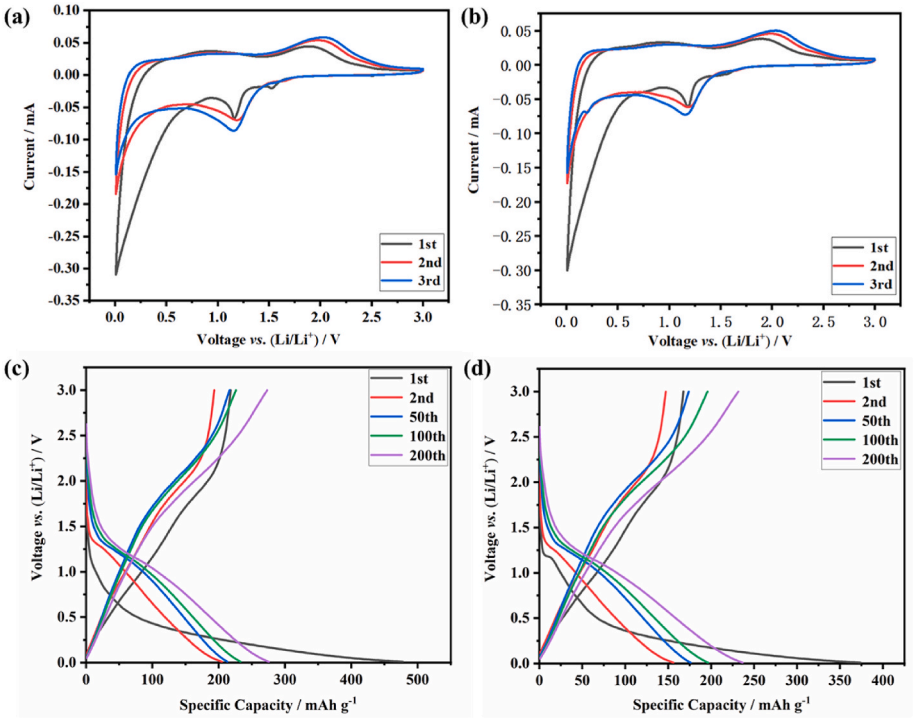

Fig. 16. Electrochemical detection: (a) cyclic voltammetry of MP; (b) cyclic voltammetry of SP; (c) charge-discharge cycle of MP; (d) charge-discharge cycle of SP.

cycles, indicating continuous changes in the activity of the anode material and an increase in active sites on the electrode surface. This behavior correlates with the gradual increase in discharge capacity observed with cycling, as shown in Fig. 16(c). The cyclic voltammogram of SP, as shown in Fig. 16(b), exhibits a redox trend similar to that of MP. The reduction peak of the sample prepared by the two powders is at 1.17 V, where Co^{2+}, Ni^{2+}, and Cu^{+} are reduced to Li_xCo, Li_xNi, and Li_xCu, respectively; oxidation peaks occur at 2.05 V, where the lithium alloys Li_xCo, Li_xNi, and Li_xCu are oxidized back to their metal ions Co^{2+}, Ni^{2+}, and Cu^{+}, as demonstrated in equations (7)–(9) [39]. For the inert element Mg, its high reduction potential leads to the formation of MgO after the first discharge, resulting in a "bystander effect." The inert MgO helps mitigate volume changes in the high-entropy oxide anode material and prevents the agglomeration of active particles, thereby enhancing the cyclic stability of the battery [40].

$$Co^{2+} + 2e^{-} + xLi \Leftrightarrow Li_xCo \tag{7}$$

$$Ni^{2+} + 2e^{-} + xLi \Leftrightarrow Li_xNi \tag{8}$$

$$Cu^{+} + 2e^{-} + xLi \Leftrightarrow Li_xCu \tag{9}$$

Fig. 16(c) illustrates that the MP achieved an initial discharge-specific capacity of 477.73 mAh g^{-1}. The Coulombic efficiency of the first charge-discharge cycle was recorded at 45.65 %. This lower initial Coulombic efficiency is attributed to the formation of a SEI layer on the surface of the electrode material and the loss of active materials, leading to irreversible capacity loss at the outset. The high initial discharge capacity can be credited to the high reactivity of various active components within the material, such as Co and Ni, with Li. After the first few cycles, the capacity stabilizes, indicating that the SEI layer has reached a stable state. The material exhibited excellent long-term cyclic performance as a lithium-ion battery anode, maintaining a Coulombic efficiency of 99.21 % even after 200 charge-discharge cycles, with no observed decay in discharge capacity. As shown in Fig. 16(d), the SP prepared via LDED achieved an initial discharge-specific capacity of 373.86 mAh g^{-1}, which is lower than that of MP. The initial charge-discharge Coulombic efficiency was 44.83 %, stabilizing at 97.98 % after 200 cycles. During the charge-discharge cycling process, the onset voltage of the discharge curves for both MP and SP gradually increased, indicating that the SEI layer on the anode became more stable over time. After 200 cycles, the capacity retention rate remained at 100 %.

4. Conclusions

In this study, (Mg, Co, Ni, Cu, Zn)O oxide ceramic specimens were successfully fabricated using laser-directed energy deposition (LDED) for the first time. The key findings are as follows.

(1) Pre-sintering Process Impact: The pre-sintering process significantly reduced porosity in the (Mg, Co, Ni, Cu, Zn)O specimens, increasing the density from 86.44 % to 96.70 %. This improvement is attributed to enhanced thermal convection in the molten pool and a more efficient gas escape, although it also introduced some cracks due to an increased CTE.
(2) Microstructure and Phase Composition: The specimens exhibited notable micro- and macro-segregation, particularly in Co and Ni, which tend to form solid solutions. The pre-sintering process further intensified segregation due to a higher thermal gradient in the melt pool. CuO was reduced in situ, resulting in Cu and Cu2O phases filling shrinkage holes.
(3) Electrochemical Performance: When used as anodes in lithium-ion batteries, both the MP and SP specimens demonstrated stable long-term cycling performance, with the MP showing a higher initial discharge capacity of 477.73 mAh g^{-1} compared to 373.86 mAh g^{-1} for the SP. However, phase segregation and uneven composition negatively impacted the overall electrochemical performance.

This work presents a novel approach for the rapid fabrication of (Mg, Co, Ni, Cu, Zn)O oxide ceramics using LDED. However, challenges such as phase segregation and suboptimal electrochemical performance compared to traditional methods remain. Future studies should focus on optimizing the oxide proportions and LDED parameters to improve the quality of high-entropy $(Mg_{0.2}Co_{0.2}Ni_{0.2}Cu_{0.2}Zn_{0.2})O$ ceramics.

CRediT authorship contribution statement

Dongjiang Wu: Writing – review & editing, Methodology, Investigation, Funding acquisition, Formal analysis, Conceptualization. **Weijie Lv:** Writing – original draft, Visualization, Validation, Methodology, Investigation, Data curation, Conceptualization. **Zheng Li:** Writing – review & editing, Validation, Investigation. **Xuexin Yu:** Writing – review & editing, Data curation. **Cong Zhou:** Resources, Funding acquisition. **Bi Zhang:** Resources, Funding acquisition. **Wei Wang:** Resources, Funding acquisition. **Huanyue Zhang:** Resources, Funding acquisition. **Guangyi Ma:** Resources, Funding acquisition. **Fangyong Niu:** Writing – review & editing, Supervision, Resources, Project administration, Methodology, Investigation, Funding acquisition, Formal analysis, Conceptualization.

Declaration of competing interest

The authors declare that they have no known competing financial interests or personal relationships that could have appeared to influence the work reported in this paper.

Acknowledgment

This work was funded by the National Natural Science Foundation of China (No. 52375312), Fundamental Research Funds for the Central Universities (No. DUT23YG230), National Key Research and Development Program of China (2023YFB4605900, 2022YFB3403401), Liaoning Province Science and Technology Plan Joint Program (2023JH2/101700299), Shenzhen Science and Technology Innovation Commission (JCYJ20210324115413036), Science Center for Gas Turbine Project (P2022-B-IV-012-001).

References

[1] C.M. Rost, E. Sachet, T. Borman, A. Moballegh, E.C. Dickey, D. Hou, J.L. Jones, S. Curtarolo, J.P. Maria, Entropy-stabilized oxides, Nat. Commun. 6 (2015) 8485, https://doi.org/10.1038/ncomms9485.
[2] G. Anand, A.P. Wynn, C.M. Handley, C.L. Freeman, Phase stability and distortion in high-entropy oxides, Acta Mater. 146 (2018) 119–125, https://doi.org/10.1016/j.actamat.2017.12.037.
[3] S.J. McCormack, A. Navrotsky, Thermodynamics of high entropy oxides, Acta Mater. 202 (2021) 1–21, https://doi.org/10.1016/j.actamat.2020.10.043.
[4] N.J. Usharani, A. Bhandarkar, S. Subramanian, S.S. Bhattacharya, Antiferromagnetism in a nanocrystalline high entropy oxide (Co, Cu, Mg, Ni, Zn)O: magnetic constituents and surface anisotropy leading to lattice distortion, Acta Mater. 200 (2020) 526–536, https://doi.org/10.1016/j.actamat.2020.09.034.
[5] D. Bérardan, S. Franger, D. Dragoe, A.K. Meena, N. Dragoe, Colossal dielectric constant in high entropy oxides, Phys. Status. Solidi-R. 10 (4) (2016) 328–333, https://doi.org/10.1002/pssr.201600043.
[6] D. Wang, S.D. Jiang, C.Q. Duan, J. Mao, Y. Dong, K.Z. Dong, Z.Y. Wang, S.H. Luo, Y.G. Liu, X.W. Qi, Spinel-structured high entropy oxide $(FeCoNiCrMn)_3O_4$ as anode towards superior lithium storage performance, J. Alloy. Compd. 844 (2020) 156158, https://doi.org/10.1016/j.jallcom.2020.156158.
[7] Z.H. Zhang, S.Z. Yang, X.B. Hu, H.D. Xu, H.G. Peng, M.M. Liu, B.P. Thapaliya, K. C. Jie, J.H. Zhao, J.X. Liu, H. Chen, Y. Leng, X.Y. Lu, J. Fu, P.F. Zhang, S. Dai, Mechanochemical nonhydrolytic sol-gel-strategy for the production of mesoporous multimetallic oxides, Chem. Mater. 31 (15) (2019) 5529–5536, https://doi.org/10.1021/acs.chemmater.9b01244.
[8] T. Jin, X.H. Sang, R.R. Unocic, R.T. Kinch, X.F. Liu, J. Hu, H.L. Liu, S. Dai, Mechanochemical-assisted synthesis of high-entropy metal nitride via a soft urea strategy, Adv. Mater. 30 (23) (2018) 1707512, https://doi.org/10.1002/adma.201707512.

[9] H.S. Nan, K.X. Song, J. Xu, S.H. Lv, S.S. Yu, X.Y. Hu, H.W. Tian, Dual-ion (de) intercalation into high-entropy perovskite oxides for aqueous alkaline battery-supercapacitor hybrid devices, Acta Mater. 257 (2023) 119174, https://doi.org/10.1016/j.actamat.2023.119174.
[10] M. Mozdzierz, J. Dabrowa, A. Stepien, M. Zajusz, M. Stygar, W. Zajac, M. Danielewski, K. Swierczek, Mixed ionic-electronic transport in the high-entropy (Co, Cu, Mg, Ni, Zn)$_{1-x}$Li$_x$O oxides, Acta Mater. 208 (2021) 116735, https://doi.org/10.1016/j.actamat.2021.116735.
[11] D. Bérardan, S. Franger, A.K. Meena, N. Dragoe, Room temperature lithium superionic conductivity in high entropy oxides, J. Mater. Chem. A 4 (24) (2016) 9536–9541, https://doi.org/10.1039/c6ta03249d.
[12] A. Sarkar, L. Velasco, D. Wang, Q.S. Wang, G. Talasila, L. de Biasi, C. Kübel, T. Brezesinski, S.S. Bhattacharya, H. Hahn, B. Breitung, High entropy oxides for reversible energy storage, Nat. Commun. 9 (2018) 3400, https://doi.org/10.1038/s41467-018-05774-5.
[13] A.D. Dupuy, X. Wang, J.M. Schoenung, Entropic phase transformation in nanocrystalline high entropy oxides, Mater. Res. Lett. 7 (2) (2019) 60–67, https://doi.org/10.1080/21663831.2018.1554605.
[14] K.P. Chen, X.T. Pei, L. Tang, H.R. Cheng, Z.M. Li, C.W. Li, X.W. Zhang, L.A. An, A five-component entropy-stabilized fluorite oxide, J. Eur. Ceram. Soc. 38 (11) (2018) 4161–4164, https://doi.org/10.1016/j.jeurceramsoc.2018.04.063.
[15] S.C. Jiang, T. Hu, J. Gild, N.X. Zhou, J.Y. Nie, M.D. Qin, T. Harrington, K. Vecchio, J. Luo, A new class of high-entropy perovskite oxides, Scripta Mater. 142 (2018) 116–120, https://doi.org/10.1016/j.scriptamat.2017.08.040.
[16] R. Djenadic, A. Sarkar, O. Clemens, C. Loho, M. Botros, V.S.K. Chakravadhanula, C. Kübel, S.S. Bhattacharya, A.S. Gandhif, H. Hahn, Multicomponent equiatomic rare earth oxides, Mater. Res. Lett. 5 (2) (2017) 102–109, https://doi.org/10.1080/21663831.2016.1220433.
[17] Z.F. Zhao, H.M. Xiang, F.Z. Dai, Z.J. Peng, Y.C. Zhou, ($La_{0.2}Ce_{0.2}Nd_{0.2}Sm_{0.2}Eu_{0.2}$)$_2Zr_2O_7$: a novel high-entropy ceramic with low thermal conductivity and sluggish grain growth rate, J. Mater. Sci. Technol. 35 (11) (2019) 2647–2651, https://doi.org/10.1016/j.jmst.2019.05.054.
[18] Y.F. Huang, D.J. Wu, D.K. Zhao, F.Y. Niu, G.Y. Ma, Investigation of melt-growth alumina/aluminum titanate composite ceramics prepared by directed energy deposition, Int. J. Extreme Manuf. 3 (3) (2021) 035101, https://doi.org/10.1088/2631-7990/abf71a.
[19] D. Wu, X. Cai, X. Qin, F. Yang, R. Kang, Z. Dong, G. Ma, Y. Bao, F. Niu, Laser ablation behavior and mechanism of Cf/C–SiC composites under different laser energy densities, Compos. B Eng. 276 (2024) 111359, https://doi.org/10.1016/j.compositesb.2024.111359.
[20] I. Kunce, M. Polanski, K. Karczewski, T. Plocinski, K.J. Kurzydlowski, Microstructural characterisation of high-entropy alloy AlCoCrFeNi fabricated by laser engineered net shaping, J. Alloy. Compd. 648 (2015) 751–758, https://doi.org/10.1016/j.jallcom.2015.05.144.
[21] Q.X. Sui, Z. Wang, J. Wang, S.R. Xu, F.J. Zhao, L. Gong, B. Liu, J. Liu, G. Liu, The microstructure and mechanical properties of the additive manufactured AlCoCrFeNi high entropy alloy, Mat. Sci. Eng. A-Struct. 833 (2022) 142507, https://doi.org/10.1016/j.msea.2021.142507.
[22] Z.J. Sun, X.P. Tan, C.C. Wang, M. Descoins, D. Mangelinck, S.B. Tor, E.A. Jägle, S. Zaefferer, D. Raabe, Reducing hot tearing by grain boundary segregation engineering in additive manufacturing: example of an Al$_x$CoCrFeNi high-entropy alloy, Acta Mater. 204 (2021) 116505, https://doi.org/10.1016/j.actamat.2020.116505.
[23] Y.F. Liu, J. Ren, S. Guan, C.Y. Li, Y. Zhang, S. Muskeri, Z.Y. Liu, D.J. Yu, Y. Chen, K. An, Y. Cao, W. Liu, Y.T. Zhu, W. Chen, S. Mukherjee, T. Zhu, W. Chen, Microstructure and mechanical behavior of additively manufactured CoCrFeMnNi high-entropy alloys: laser directed energy deposition versus powder bed fusion, Acta Mater. 250 (2023) 118884, https://doi.org/10.1016/j.actamat.2023.118884.
[24] J.M. Joubert, Y. Kalchev, A. Fantin, J.C. Crivello, R. Zehl, E. Elkaim, G. Laplanche, Site occupancies in a chemically complex s-phase from the high-entropy Cr-Mn-Fe-Co-Ni system, Acta Mater. 259 (2023) 119277, https://doi.org/10.1016/j.actamat.2023.119277.
[25] O.A. Lukianova, V. Kulitckii, Z. Rao, Z. Li, G. Wilde, S.V. Divinski, Self-diffusion in carbon-alloyed CoCrFeMnNi high entropy alloys, Acta Mater. 237 (2022) 118136, https://doi.org/10.1016/j.actamat.2022.118136.
[26] D.K. Zhao, D.J. Wu, J. Shi, F.Y. Niu, G.Y. Ma, Microstructure and mechanical properties of melt-grown alumina-mullite/glass composites fabricated by directed laser deposition, J. Adv. Ceram. 11 (1) (2022) 75–93, https://doi.org/10.1007/s40145-021-0518-6.
[27] X.X. Yu, D.J. Wu, W.M. Bi, X. Feng, Z.Y. Zhao, Y.B. Hao, G.Y. Ma, C. Zhou, F.Y. Niu, Direct additive manufacturing of Al_2O_3-TiCp functionally graded ceramics by laser-directed energy deposition, J. Am. Ceram. Soc. 107 (5) (2024) 3522–3533, https://doi.org/10.1111/jace.19653.
[28] Y.F. Huang, D.J. Wu, C.X. Li, W.J. Lv, G.Y. Ma, C. Zhou, F.Y. Niu, Investigation on the cracking mechanism of melt growth alumina/aluminum titanate ceramics prepared by laser directed energy deposition, Chin. J. Mech. Eng.: Addit. Manuf. 2 (4) (2023) 100099, https://doi.org/10.1016/j.cjmeam.2023.100099.
[29] D.J. Wu, H.C. Liu, F. Lu, G.Y. Ma, S. Yan, F.Y. Niu, D.M. Guo, Al_2O_3-YAG eutectic ceramic prepared by laser additive manufacturing with water-cooled substrate, Ceram. Int. 45 (3) (2019) 4119–4122, https://doi.org/10.1016/j.ceramint.2018.11.032.
[30] H.J. Su, J. Zhang, L. Liu, J. Eckert, H.Z. Fu, Rapid growth and formation mechanism of ultrafine structural oxide eutectic ceramics by laser direct forming, Appl. Phys. Lett. 99 (22) (2011) 221913, https://doi.org/10.1063/1.3664108.
[31] D.J. Wu, X.X. Yu, Z.Y. Zhao, G.Y. Ma, C. Zhou, B. Zhang, G.H. Ren, J. Han, H. Wang, F.Y. Niu, Direct additive manufacturing of TiCp reinforced Al_2O_3-ZrO_2 eutectic functionally graded ceramics by laser directed energy deposition, J. Eur. Ceram. Soc. 43 (6) (2023) 2718–2723, https://doi.org/10.1016/j.jeurceramsoc.2022.12.068.
[32] X.X. Yu, D.J. Wu, X. Feng, C. Zhou, B. Zhang, H.Y. Zhang, Q. Bai, G.Y. Ma, F.Y. Niu, One-step additive manufacturing of melt-growth porous ceramics by laser directed energy deposition, J. Eur. Ceram. Soc. 44 (2024) 116748, https://doi.org/10.1016/j.jeurceramsoc.2024.116748.
[33] W.C. Hong, F. Chen, Q. Shen, Y.H. Han, W.G. Fahrenholtz, L.M. Zhang, Microstructural evolution and mechanical properties of (Mg, Co, Ni, Cu, Zn)O high-entropy ceramics, J. Am. Ceram. Soc. 102 (4) (2019) 2228–2237, https://doi.org/10.1111/jace.16075.
[34] J.A. Spencer, A.L. Mock, A.G. Jacobs, M. Schubert, Y.H. Zhang, M.J. Tadjer, A review of band structure and material properties of transparent conducting and semiconducting oxides: Ga_2O_3, Al_2O_3, In_2O_3, ZnO, SnO_2, CdO, NiO, CuO, and Sc_2O_3, Appl. Phys. Rev. 9 (1) (2022) 011315, https://doi.org/10.1063/5.0078037.
[35] C.M. Rost, D.L. Schmuckler, C. Bumgardner, M.S. Bin Hoque, D.R. Diercks, J. T. Gaskins, J.P. Maria, G.L. Brennecka, X.D. Li, P.E. Hopkins, On the thermal and mechanical properties of $Mg_{0.2}Co_{0.2}Ni_{0.2}Cu_{0.2}Zn_{0.2}O$ across the high-entropy to entropy-stabilized transition, Apl. Mater. 10 (12) (2022) 121108, https://doi.org/10.1063/5.0122775.
[36] K.G. M., F.G. K., Thermodynamic Models for Industrial Applications: from Classical and Advanced Mixing Rules to Association Theories, John Wiley & Sons, 2009, https://doi.org/10.1002/9780470747537.
[37] U. Mizutani, Hume-rothery Rules for Structurally Complex Alloy Phases, CRC Press, Florida, 2010, pp. 323–399, https://doi.org/10.1142/9789814304771_0011. Taylor and Francis.
[38] F.X. Zhang, S.J. Zhao, K. Jin, H. Xue, G. Velisa, H. Bei, R. Huang, J.Y.P. Ko, D. C. Pagan, J.C. Neuefeind, W.J. Weber, Y.W. Zhang, Local structure and short-range order in a NiCoCr solid solution alloy, Phys. Rev. Lett. 118 (20) (2017) 205501, https://doi.org/10.1103/PhysRevLett.118.205501.
[39] A.K. Mondal, D.W. Su, S.Q. Chen, X.Q. Xie, G.X. Wang, Highly porous $NiCo_2O_4$ nanoflakes and nanobelts as anode materials for lithium-ion batteries with excellent rate capability, Acs Appl. Mater. Inter. 6 (17) (2014) 14827–14835, https://doi.org/10.1021/am5036913.
[40] N. Qiu, H. Chen, Z.M. Yang, S. Sun, Y. Wang, Y.H. Cui, A high entropy oxide ($Mg_{0.2}Co_{0.2}Ni_{0.2}Cu_{0.2}Zn_{0.2}O$) with superior lithium storage performance, J. Alloy. Compd. 777 (2019) 767–774, https://doi.org/10.1016/j.jallcom.2018.11.049.